Acta Astronautica 213 (2023) 252–263

Contents lists available at ScienceDirect

Acta Astronautica

journal homepage: www.elsevier.com/locate/actaastro

Research paper

Electro-optical characterization of a novel surface DBD plasma actuator operating in typical gas rarefaction conditions of near-space applications

D. Fontanarosa [a,d], M.A. Signore [b], A.M. Toscano [a], M.G. De Giorgi [a,*], E. Pescini [c], A. Ficarella [a], L. Francioso [b]

[a] Department of Engineering for Innovation, University of Salento, via per Monteroni, Lecce I-73100, Italy
[b] Italian National Research Council - Institute for Microelectronics and Microsystems, Via per Monteroni "Campus Ecotekne", Lecce, Italy
[c] Centro Universitario de la Defensa, Universidad Politécnica de Cartagena, C/Coronel López Peña S/N, Santiago de La Ribera, 30720 Murcia, Spain
[d] KU Leuven, Department of Mechanical Engineering, Division of Applied Mechanics and Energy Conversion (TME), B-3001 Leuven, Belgium

ARTICLE INFO

Keywords:
Air-breathing electric propulsion
Active flow control
Plasma actuation
Micro-manufacturing
Surface DBD

ABSTRACT

The present work provides an experimental investigation of a novel surface dielectric barrier discharge plasma actuator consisting of a 0.3 mm-thick alkali-free quartz substrate as dielectric barrier material and titanium-tungsten electrodes. The device is manufactured using ultraviolet lithography and CMOS processes, and experiments are conducted under sinusoidal plasma actuation in a vacuum chamber with pressure ranging from 20 kPa to 0.01 Pa. Intensified high-speed visualizations of the plasma discharge and electrical signals (current/voltage/power) define the diagnostic toolbox. Results highlight that at 20 kPa the plasma discharge is driven by the formation of micro sparks on the inner edge of the exposed electrode, propagating downstream in larger current structures. At 1 kPa, the plasma discharge becomes more glow-type with negative current regimes longer than the positive ones, while the voltage signals preserve their sinusoidal shape. In such a plasma regime, the discharge extends over the entire region covered by the electrodes, suggesting the use of larger grounded electrodes to further enlarge the actuation region. Furthermore, the momentum action of the plasma discharge is not anymore unidirectional as it acts on the whole device plane. At pressure between 50 Pa and 2.5 Pa, the plasma discharge is unstable exhibiting a fast modification of the plasma discharge. Below 2.5 Pa, it becomes a volumetric full glow-type, extending its action mainly upstream with a higher plasma density on the exposed electrode. The establishment of the new plasma regime at a pressure below 2.5 Pa affects the electrical dissipated power and asymmetry of voltage and current signals.

1. Introduction

According to [1], near-space, typically ranging from approximately 20 to 100 kilometres above the Earth's surface, provides opportunities for exploration, meteorological research, and payload delivery to low Earth orbit. There is increasing interest in developing propulsion systems for long-duration, high-altitude platforms in this region. However, traditional airbreathing jet engines are inefficient at such altitudes, and ion engines face challenges due to high atmospheric pressure [2]. Electric propulsion systems have gained widespread use in various applications. They play a crucial role in functions like station keeping [3], drag compensation [4], and attitude control for satellites in geostationary orbit (GEO) and low Earth orbit (LEO) [2]. Near-space poses unique challenges due to atmospheric conditions and density. These conditions hinder the effective use of traditional electric propulsion systems. Limitations arise from the need to carry the working medium, which hampers long-term missions, and the lack of optimization for atmospheric operation. Consequently, direct utilization of space electric propulsion systems for near-space missions is impractical. Recent research has focused on micro-jet systems for near-space applications [5,6]. Electrohydrodynamic (EHD) propulsion systems, utilizing non-thermal non-equilibrium low-temperature plasma generated by corona discharge or dielectric barrier discharge (DBD) plasma actuators (PAs), offer a promising solution to these challenges [7,8]. These plasma actuators ionize and accelerate gas, generating thrust as an alternative to conventional space electric propulsion systems unsuitable for near-space [9]. In corona discharge-based EHD systems, the setup

* Correspondence to: Department of Engineering for Innovation, Research Center for Energy and Environment (UNISALENTO-DII-CREA), University of Salento, via per Monteroni, Lecce I-73100, Italy.
E-mail addresses: donato.fontanarosa@kuleuven.be (D. Fontanarosa), mariaassunta.signore@cnr.it (M.A. Signore), angelicamaria.toscano@unisalento.it (A.M. Toscano), mariagrazia.degiorgi@unisalento.it (M.G. De Giorgi), elisa.pescini@cud.upct.es (E. Pescini), antonio.ficarella@unisalento.it (A. Ficarella), lucanunzio.francioso@cnr.it (L. Francioso).

https://doi.org/10.1016/j.actaastro.2023.09.003
Received 1 June 2023; Received in revised form 23 July 2023; Accepted 2 September 2023
Available online 7 September 2023

Nomenclature

Symbols

a_i	Temporal eigenfunction of POD mode i, [a.u]
B	Image luminance, [a.u.]
f_{elec}	Actuation frequency, [Hz] or [kHz]
I	Electrical current, [A] or [mA]
L_{eff}	Effective electrode span length, [m
L_{nom}	Nominal electrode span length, [m]
L_{pd}	Plasma discharge length, [mm]
N_{img}	Number of processed images, [count]
N_{POD}	Number of POD modes, [count
p_a	Vacuum level, [Pa] or [kPa]
P_{el}	Electrical power, [W]
p_{pd}	Power discharge power density, W/kg/m^2
r	Electrodes overlap, [m]
t	Time variable, [s]
t_1	Exposed electrode thickness, [nm]
t_2	Covered electrode thickness, [nm]
t_d	Dielectric substrate thickness, [m]
V_{app}	Applied voltage, [V] or [kV]
w_1	Exposed electrode width, [m]
w_2	Covered electrode width, [m]

Greek Symbols

Δt_v	Actuation period, [s]
$\delta_{(\cdot)}$	Absolute uncertainty of the quantity $(\cdot)$
Λ_i	Relative POD energy of mode i, [a.u]
λ_i	Eigenvalue of POD mode i, [a.u]
ϕ_i	Spatial eigenfunction of POD mode i, [a.u]
ρ_B	Image luminance density, [a.u./count]
σ_B	Standard deviation of the image luminance, [a.u.]

Subscripts

avg	Referred to the average value
pp	Referred to the peak-to-peak value
$smXYZ$	Referred to smoothed signals using moving average window of size equal to XYZ (integer number) samples

Abbreviations

AFM	Atomic Force Microscopy
CD	Corona Discharge
CMOS	Complementary Metal–Oxide–Semiconductor
CNR-IMM	Italian National Research Council — Institute for Microelectronics and Microsystems
EHD	ElectroHydroDynamics
HV	High Voltage
iCCD	Intensified Charge-Coupled Device
JAXA	Japan Aerospace Exploration Agency
PA	Plasma Actuator
POD	Proper Orthogonal Decomposition
PTFE	Poly Tetra Fluoro Ethylene
SDBD	Surface Dielectric Barrier Discharge
VLEO	Very Low Earth Orbit

includes an anode (emitter), ionization zone, ion drift zone, and cathode (collector) working together to generate thrust. Gas ionization occurs near the anode under a strong electric field, and in the drift zone, ions transfer energy to the propellant through collisions with neutral particles. As the ions reach the cathode and undergo deionization, they continue neutrally with the fluid flow, resulting in thrust production upon fluid exit [10].

Regarding EHD systems based on DBD discharge, the Surface Dielectric Barrier Discharge Plasma Actuator (SDBD-PA) offers a simple configuration. It consists of two metallic electrodes on opposite faces of a dielectric substrate in a planar setup. One electrode is supplied with a high-voltage (HV) waveform, exposed to the flow, while the other is grounded, encapsulated by dielectric material with a controlled shift [11]. There are typically two modes of operation. One involves repetitive HV pulses, nanoseconds wide with frequencies ranging from a few hundred hertz to a few hundred kilohertz. Fast localized gas heating generates pressure or shock waves, and the repetition of pulses creates pressure oscillations for flow separation control, often with a direct current/alternating current (DC/AC) bias [12]. Conventional DBD-PA operation utilizes an AC voltage waveform (amplitude 5–20 kV) in the frequency range of approximately 1–20 kHz. A sinusoidal excitation voltage applied to the exposed electrode creates a robust electric field between the two electrodes. Collision ionization occurs within the gas molecules, causing charged particles to move directionally under the electric field. These charged particles then collide with nearby neutral particles, inducing an airflow from the upper to the lower electrode [13]. Ukai et al. [14] experimentally investigated the spatial distribution of density associated with a nanosecond pulsed dielectric barrier discharge plasma actuator (ns-DBD-PA). Schlieren techniques showed the formation and movement of a hot plume originating from the exposed electrode. The plasma-induced flow became apparent after the initial discharges, with subsequent discharges increasing the density until reaching a quasi-steady state.

The EHD force generated by SDBD-PA shares similarities with the ionic wind produced in corona discharge. PAs offer advantages for near-space applications. Firstly, they ionize gas, creating plasma, and generate thrust using the resulting electric field. This eliminates the need for propellant expulsion seen in conventional systems, enabling efficient operation in the low-density near-space environment. Secondly, EHD actuators provide precise control over thrust. Electric field parameters like voltage and frequency can be adjusted to regulate the PA's thrust. This control is vital for maneuvering and stabilizing near-space vehicles, adapting to atmospheric conditions and performing delicate operations. PAs are also lightweight and compact, suitable for near-space where weight and size are critical. Their compactness allows easy integration into small-scale vehicles without compromising payload or mission objectives.

Additionally, the absence of propellant mass expulsion reduces the dependency on consumable resources and extends the operational lifespan of near-space vehicles utilizing plasma actuators. This advantage is particularly relevant for prolonged missions or deployments where resupplying propellant is impractical or costly. As a conclusion, can be affirmed that their ability to generate thrust in low-density environments, precise control, compactness, and reduced propellant dependency make them well-suited for near-space vehicles. However, it is important to note that PAs also present some challenges and limitations. For instance, the thrust generated by plasma actuators is typically lower compared to conventional propulsion systems, which may limit their application to certain types of near-space missions. The efficiency and scalability of plasma actuators for larger-scale vehicles or longer-duration missions are still areas of ongoing research and development.

Research on DBD-PAs mainly encompassed actuator design and performance [15,16], flow field evolution during discharge [14], and flow separation control [17]. Efforts aim to uncover their potential and effectiveness in various applications. Refining actuator design,

including optimizing geometry, electrode configuration, and overall structure, has been a particular focus. Exploring different electrode shapes, sizes, quantities, and arrangements aims to achieve desired flow control effects and maximize operational efficiency. In the study [15], an innovative design approach was explored, using multi-encapsulated electrodes to enhance plasma actuator performance, i.e. higher velocities and increased momentum in the surrounding air. In [18], increasing the applied voltage to a double-encapsulated electrode DBD-PA caused the plasma to expand over the dielectric surface, starting from the edge of the exposed electrode. Bright patches at the electrode edge indicated weaknesses in the actuator construction, where points of high electric stress ignited the plasma first, resulting in brighter areas in time-exposed images. The overall plasma distribution appeared uniform with a slight brightness gradient, as the edge plasma had been present for a shorter time. At the highest applied voltage (16 kV peak-to-peak), coarse filaments, originating from regions of high electrical stress, were present. Operating the plasma actuators in this filamentary mode led to performance degradation and reduced actuator lifespan. PAs performance is affected by various environmental conditions [11,19]. In [19], the effect of external flow on actuator performance, particularly in high-speed unsteady flows encountered in flight environments, was investigated. Results revealed that the plasma influences not only the external shear layer of the shock tube but also the shock front passage, significantly affecting plasma properties. In-flight applications, external factors such as temperature, pressure, and humidity can vary, impacting the discharge parameters of PAs. Few studies investigated the effect of low pressure, typically of near-space applications, on the plasma discharge evolution and PA performance. In low-pressure discharge, plasma density is low, hindering effective field shielding. Charges separate, and high-velocity electrons vanish at the extremities, leaving a higher density of positive ions. Reverse discharge yields higher positive ion density than forward discharge, with volume force from ion-neutral collisions.

A recent study by Wojewodka et al. [20] characterized the behaviour of a ns-DBD-PA using Schlieren imaging at varying ambient pressures (30–100 kPa). Shock wave speed and intensity were recorded, showing trends with decreasing ambient pressure. Higher pressures resulted in stronger shock waves, irrespective of actuator thickness, likely due to fewer air molecules for ionization at lower pressures. Dielectric barrier thickness also influenced shock wave intensity, with thinner barriers producing stronger shocks. This study emphasizes the importance of considering ambient pressure and dielectric barrier thickness in ns-DBD-PA performance, particularly in altitude applications. Environmental conditions influence the performance also of corona discharge-based EHD PAs. The study [21] reveals a relationship between thrust and pressure at a constant applied voltage. Initially, increasing pressure from 0.05 atm to 0.5 atm decreases thrust, followed by an increase. However, further increasing pressure from 0.5 atm to 1 atm leads to a decrease in thrust. The study shows the voltage's influence on the pressure at which thrust reaches maximum. Higher voltage applied to the EHD-PA increases the pressure to reach the maximum thrust. Xu et al. [22] studied the performance of an air-breathing electric thruster using SDBD technology under low-pressure conditions. Their research discovered a nonmonotonic relationship between pressure and thrust. Literature studies also indicate that the electrokinetic energy conversion efficiency of the SDBD thruster is significantly low at atmospheric pressure (0.1 MPa). In fact, its efficiency is less than 1%, indicating room for improvement in terms of energy conversion efficiency [23,24]. According to Bernard [25], a flat DBD actuator, powered by a sinusoidal voltage source at pressures as low as 0.2 atm, exhibited 40 mN/m thrust per unit length. They also achieved a thrust-to-power ratio of 0.6 mN/W. Soni [26] studied the behaviour of DBD within the pressure range of 13–101 kPa, revealing a pressure point where maximal thrust was achieved. At a pressure of 0.2 atm, the specific thrust reached 5 mN/m. Bottelberghe et al. [27] observed plasma actuator discharge performance and airflow velocities

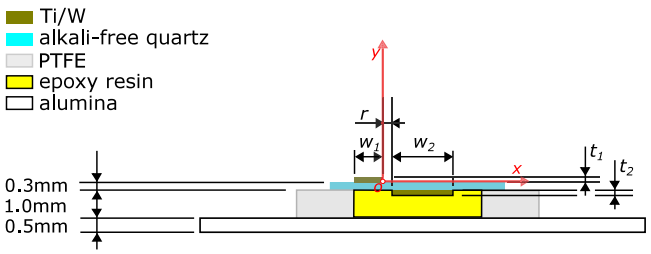

Fig. 1. SDBD-PA configuration: 2D cross-sectional view.

at pressures of 0.4–1 atm, finding a minimum pressure thrust of 0.2 mN/m. Wu [28] proposed and validated a theoretical thrust model through experiments within a pressure range of 10–90 kPa, achieving a thrust density of 16 mN/m.

Based on the context discussed above, the behaviour of the plasma discharge produced by an SDBD-PA is still unexplored under typical gas rarefaction conditions of near-space applications with pressures below a few kilopascals. Furthermore, the gas-rarefied condition and the consequent collisional phenomena significantly increase the complexity of the physics and chemistry involved in such a plasma discharge. This couples with the need for reduced order models of SDBD-PAs to improve the predictability of the plasma discharge, which requires experimental data to be processed with techniques which can extrapolate the most relevant information into the domains of space–time–frequency. All of the existing limitations outlined above are addressed in the present work by providing an electro-optical characterization of the plasma discharge undergoing in the vacuum range 20 kPa–0.01 Pa. To this purpose, an innovative SDBD-PA was designed and fabricated by the Institute for Micro-electronics and Micro-systems of the Italian National Research Council (CNR-IMM) (Italy) using ultraviolet lithography and complementary metal–oxide–semiconductor (CMOS) technology, which allowed an advanced device engineering via the integration of a titanium nitride coating over the tungsten high-voltage electrodes to mitigate their degradation and extend the device's lifetime. Two vacuum ranges were investigated, i.e. intermediate vacuum from 20 kPa up to 1 kPa, and high vacuum from 1100 Pa up to 0.01 Pa. In the intermediate vacuum conditions, intensified high-speed visualizations allowed for an extensive topological and statistical (via proper orthogonal decomposition) space–time characterization of the plasma discharge, in combination with the analysis of electrical signals. The analysis of electrical signals was then extended to the high vacuum level, coupled with an analysis of plasma discharge appearance as a function of the gas rarefaction level. Finally, this paper addressed the scarcity of plasma actuator degradation studies under low-pressure conditions. As such, a qualitative analysis was performed using Atomic Force Microscopy to investigate the impact of the plasma discharge on the degradation of the plasma actuator device. Specifically, the influence of plasma bombardment on the roughness of the HV electrode and glass substrate was analysed in detail.

2. Device description, manufacturing and preparation

The dielectric selected for the project activity was the alkali-free quartz AF32@eco by SCHOTT [29]. The manufacturing process was carried out at CNR-IMM clean room facilities. The 300 μm thick AF-32 glass substrates were cleaned in acetone ultrasonic bath and then rinsed in deionized water, followed by hotplate dehydration at 120 °C for 300 s. The glass surface organic contaminants were removed by a 10 min oxygen plasma treatment at 1 Torr of absolute pressure. The patterning of the front (exposed) and backside (grounded) metal layers was realized by 365 nm optical lithography followed by lift-off technique. Deposition of 200 nm thick tungsten (W) on the front side and 400 nm on the backside of the samples were performed by

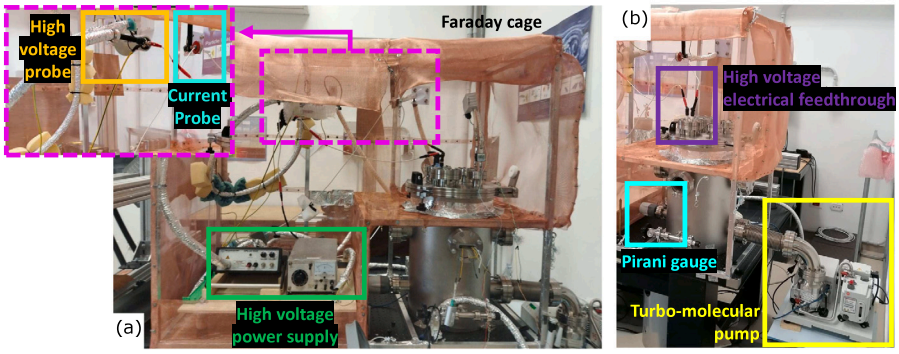

Fig. 2. Vacuumed plasma discharge facility at University of Salento: (a) frontal view; (b) side view.

Table 1
Geometrical characteristics of the SDBD-PA.

SDBD-PA geometrical characteristics	Value
nominal electrode span length, L_{nom} [m]	0.030
effective electrode span length, L_{eff} [m]	0.026
exposed electrode width, w_1 [m]	0.005
exposed electrode thickness, t_1 [nm]	210
covered electrode width, w_2 [m]	0.015
covered electrode thickness, t_2 [nm]	400
electrodes overlap, r [m]	0.002
dielectric thickness, t_d [m]	0.0003

direct current magnetron sputtering. A 10 nm thick adhesion layer of titanium (Ti) was deposited on glass before W deposition. After substrate dicing, a single SDBD-PA was packaged onto a polytetrafluoroethylene (PTFE) carrier holder with epoxy resin, sealing the ground electrode and electrical connections. Fig. 1 shows the drawing of the final operational configuration that was tested. To increase strength and manoeuvrability the devices have been equipped with a 0.5 mm alumina layer. Table 1 summarizes the geometric characteristics of the designed SDBD-PA. Atomic force microscopy topography images were acquired over the maximum entire scan area of $100\,\mu m^2$ (resolution of 256 × 256 points) and the roughness has been calculated as the mean value of ten scans over the maximum scan area. The topography has been acquired over an area of $10\,\mu m^2$ too, to appreciate better the surface features. To this purpose, a Nanosurf CoreAFM instrument was employed, operating in contact mode, at room temperature and in air environment. A monolithic silicon probe tip with chromium/platinum reflective coating (MULTI75-EG) was used at the typical resonance frequency of 75 kHz, with a constant force of 3 N/m.

3. Experimental setup and methodology

Experiments have been performed in the vacuumed plasma discharge facility at the University of Salento (Italy), shown in Fig. 2. It consists of a vertical cylindrical vacuum chamber with a diameter of about 0.35 m and a length equal to about 0.5 m. It is equipped with two quartz windows perpendicular to the chamber axis ensuring the optical access into the chamber, while a high-voltage electrical feedthrough is located on the top cover of the chamber. The pressure inside the vacuum chamber was controlled using a turbo-molecular pumping system Edwards T-Station 85H Wet ISO63 coupled with a Pirani gauge model Edwards WRG-S-DN40CF and the needle leak valve LV10K. Vacuum levels above 1 kPa were measured using the digital vacuum meter model Pneumax DS.60.V.I.F1.F.0 (accuracy of ±1 kPa) installed on the top flange of the vacuum chamber.

Concerning the electrical feeding, a sinusoidal high frequency/HV signal was provided to the HV electrode using an HV generator (model PVM500 Plasma Resonant and Dielectric Barrier Corona Driver). The applied voltage signal was acquired using the HV probe Tektronix P6015 A (accuracy of ±3% of reading). The current transformer Bergoz model CT-C1.0-BNC was used, instead, to measure the current flowing in the circuit with an accuracy of ±0.5% of reading. Both the HV probe and the current transformer signals were simultaneously acquired using the oscilloscope model Rohde&Schwarz RTM3004 (accuracy of ±3% of reading). The acquisition sample rate was set to 1.2 GHz and each acquisition was given by averaging 256 samples. The overall electrical setup was properly placed inside a Faraday cage made of a copper fine wire mesh. Based on voltage and current measurements, the electrical dissipated power of the SDBD-PA P_{el} was computed as follows:

$$P_{el} = \frac{1}{\Delta t_V} \int_0^{\Delta t_V} V_{app}(t)\, I(t)\, dt \tag{1}$$

where Δt_V is the actuation period, while $I(t)$ and $V_{app}(t)$ are the acquired current and the voltage signals, respectively. The numerical integration was performed via the trapezoidal method. For steady-state measurements, the average value of the dissipated power $P_{el,avg}$ was calculated by averaging $3n$ consecutive power measurements. The absolute uncertainty of each acquired P_{el} was retrieved by sequentially perturbing the input variables in Eq. (1) and accumulating the individual uncertainty contributions coming from the measurement equipment (i.e, oscilloscope, current and voltage probes), as described in [30, p. 5]. Therefore, the overall absolute uncertainty of $P_{el,avg}$, δ_P resulted from the root mean square method [30, Eq. 4] applied to the averaging function.

3.1. Plasma discharge imaging

The optical setup is shown in Fig. 3(a). It consists of the high-speed camera Phantom M320S equipped with the image intensifier Lamber HiCATT, thus obtaining an intensified charge-coupled device (iCCD) camera. The camera system was installed in front of the SDBD-PA exposed electrode with optical axis perpendicular to the quartz window of the vacuum chamber (see Fig. 3(b)). The SDBD-PA was mounted on a micrometric linear stage for fine vertical positioning, and it was used as a target for spatial calibration (calibration factor equal to about 5×10^{-5} m/pixel). The intensifier gain and gate were set to 850 and 2.5 µs, respectively. The iCCD camera was paired with a 78 mm ultraviolet lens with an aperture set to f/3.8. For each test the camera acquired a data set consisting of 1000 greyscale images at about 983.9 Hz, resulting in a phase-locked acquisition (1 frame captured every 21 actuation cycles). The greyscale was discretized through 12 bits, which correspond to a range from 0 (full darkness condition) to 4095 (full brightness condition). The extremes of the range respectively represent the condition of absolute darkness (very low luminosity) and the condition of full brightness (high luminosity). User-defined Matlab® routines allowed for the post-processing of the image dataset as described in the following. The electromagnetic radiation of the plasma discharge and, hence, its intensity, is proportional to the image

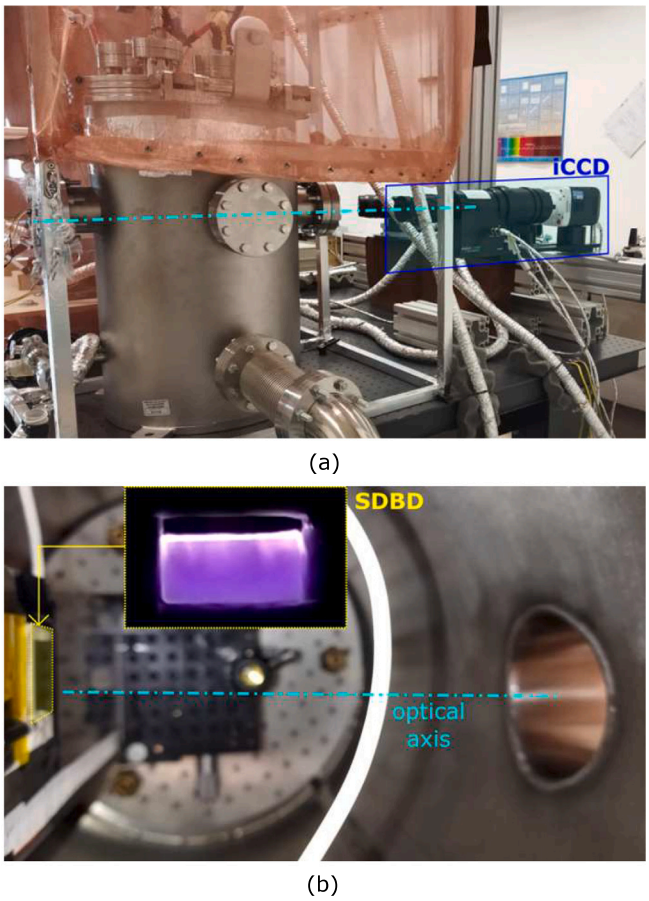

Fig. 3. Experimental optical setup: (a) location and orientation of the iCCD camera; (b) SDBD-PA vertically mounted in front of the optical window.

luminance. Therefore, the time-averaged luminance was retrieved first from the collected image dataset, by applying Eq. (2):

$$B_{avg}(x_i, z_i) = \frac{1}{N_{img}} \sum_{k=1}^{N_{img}} B(x_i, z_i, t_k) \tag{2}$$

where t_k is the kth time frame, N_{img} is the number of images of the dataset and (x_i, z_i) are the coordinates identifying the generic pixel point $R(x_i, z_i)$. The standard deviation σ_B was also computed with Eq. (3) to map the temporal dispersion of the acquired plasma discharge luminance with respect to the time-averaged value previously retrieved:

$$\sigma_B(x_i, z_i) = \frac{1}{N_{img} - 1} \sqrt{\sum_{k=1}^{N_{img}} |B(x_i, z_i, t_k) - B_{avg}(x_i, z_i)|^2} \tag{3}$$

In addition, the global temporal signal of the image luminance density was extrapolated by applying to each image the threshold of $B > 50$ (noise removal) and computing the spatially averaged luminance value as follows:

$$\rho_{B>50}(t_k) = \frac{1}{N_{px}(t_k)} \sum_i B(x_i, z_i, t_k) \Big|_{B>50} \tag{4}$$

where $N_{px,B>50}(t_k)$ is the number of image pixel points $R(x_i, z_i)$ of the time frame t_k satisfying the threshold condition $B > 50$. The resulting signal $\rho_{B>50}(t_k)$ was then smoothed using a moving window averaging with a span equal to 15 samples, thus obtaining the final image luminance density signal $\rho_{B>50,sm15}$.

Furthermore, the proper orthogonal decomposition (POD) has been applied to the iCCD dataset, carrying out a modal spatio-temporal characterization of the observed plasma discharge dynamics. The authors refer to Sirovich [31] and Tropea et al. [32] for a detailed description of the technique, which is far from the scope of the present work. Briefly, the POD extracts an orthogonal basis of eigenvalues from the generic flow data field $g(\boldsymbol{x}, t)$ decoupling the spatial and temporal contributions, that is:

$$g(\boldsymbol{x}, t) = \sum_l g_l(\boldsymbol{x}, t) = \sum_l \phi_l(\boldsymbol{x})\, a_l(t) \tag{5}$$

where $a_l(t)$ is the lth temporal eigenfunction, $\phi_l(\boldsymbol{x})$ represents the lth spatial eigenfunction, and $\boldsymbol{x}$ denotes the vector of the spatial coordinates. $a_l(t)$ collects information about the dynamics of the modal coherent structures, $\phi_l(\boldsymbol{x})$ consists of a picture of the flow able to capture the scales and shapes of the modal coherent structures. The relative energy contribution in image reconstruction related to the lth POD mode is defined as:

$$\Lambda_l = \frac{\lambda_l}{\sum_j^{N_{POD}} \lambda_j} \tag{6}$$

where λ_l is the lth eigenvalue of the autocorrelation tensor of the given flow field data. As specified in Kypraiou et al. [33], two different approaches to POD can be distinguished based on the combination of averaging and correlation, namely the classic or direct method (Lumley [34]), which is based on the temporal averaging and spatial correlation, or the snapshot method (Sirovich [31]) that uses the spatial averaging and the temporal correlation instead. In the present work, the latter has been applied for the analysis of the plasma discharge dynamics, since it is suitable when the data field has a good spatial resolution but a relatively short time history. By using this approach, the size of the eigenvalue problem is given by the number of the field snapshots, i.e. $N_{POD} = N_{img}$.

4. Results and discussion

This section presents the results of the electrical characterization of the SDBD plasma discharge in two vacuum ranges: steady-state analysis of the intermediate vacuum from 20 kPa to 1 kPa using iCCD acquisitions and electrical signals (Section 4.1), and transient analysis of the high vacuum from 1100 Pa to 0.01 Pa using electrical signals and photo-sequence of the plasma discharge appearance (Section 4.2).

4.1. Intermediate vacuum: 20 kPa to 1 kPa

Acquisitions started 300 s after the beginning of the plasma actuation at constant actuation frequency $f_{elec} = 20.1$ kHz. The average electrical dissipated power $P_{el,avg}$, peak-to-peak voltage $V_{pp,avg}$, and peak-to-peak current $I_{pp,avg}$, are reported in Table 2 together with their absolute uncertainties denoted by the symbol δ. It is worth outlining that the maximum relative uncertainties are 8.11% in $V_{pp,avg}$, and 6.67% in both $I_{pp,avg}$ and $P_{el,avg}$.

Fig. 4 shows the time-averaged (on the left) and the standard deviation (on the right) images of the plasma discharge luminance captured by the iCCD. This last one is used to estimate the discharge length L_{pd} (denoted by the dash-dotted magenta line) by considering the luminance threshold $\sigma_B > 100$. Therefore, the average discharge power density $p_{pd,avg}$ is retrieved as in Eq. (7) (maximum relative uncertainty equal to 9.52%), by supposing constant the thickness of the plasma discharge and taking into account the vacuum level p_a, the ambient temperature $T_{amb} = 298$ K, the specific gas constant of air $R_{air} = 287$ J/kg/K:

$$p_{pd,avg} = \frac{P_{el,avg}}{\left[\frac{p_a}{R_{air} T_{amb}}\right] L_{pd}} \tag{7}$$

Results show that the peak-to-peak voltage reduces with vacuum level as a consequence of the resistive-capacitive-inductive behaviour of the overall electrical circuit including the SDBD-PA. In this regard, it is worth observing that all experiments have been conducted using

Table 2
Electrical performance of the SDBD-PA at f_{elec} = 20.1 kHz as a function of the vacuum level p_a. Peak-to-peak voltage: average $V_{pp,avg}$ and absolute uncertainty $\delta_{V\,pp}$. Peak-to-peak current: average $I_{pp,avg}$ and absolute uncertainty $\delta_{I\,pp}$. Dissipated power: average $P_{el,avg}$ and absolute uncertainty δ_P. Plasma discharge length L_{pd} and absolute uncertainty $\delta_{L,pd}$. Average discharge power density $p_{pd,avg}$ and absolute uncertainty $\delta_{p_{pd}}$.

p_a [kPa]	$V_{pp,avg}$ [kV]	$\delta_{V\,pp}$ [kV]	$I_{pp,avg}$ [mA]	$\delta_{I\,pp}$ [mA]	$P_{el,avg}$ [W]	δ_P [W]	L_{pd} [mm]	$\delta_{L,pd}$ [mm]	$p_{pd,avg}$ [W/kg/m^2]	$\delta_{p_{pd}}$ [W/kg/m^2]
20	3.7	±0.3	214	±6	3.0	±0.2	7.31	±0.05	2200	200
5	2.24	±0.08	104	±5	1.31	±0.08	10.75	±0.05	2100	200
1	1.95	±0.08	45	±3	1.21	±0.05	12.5	±0.05	8000	600

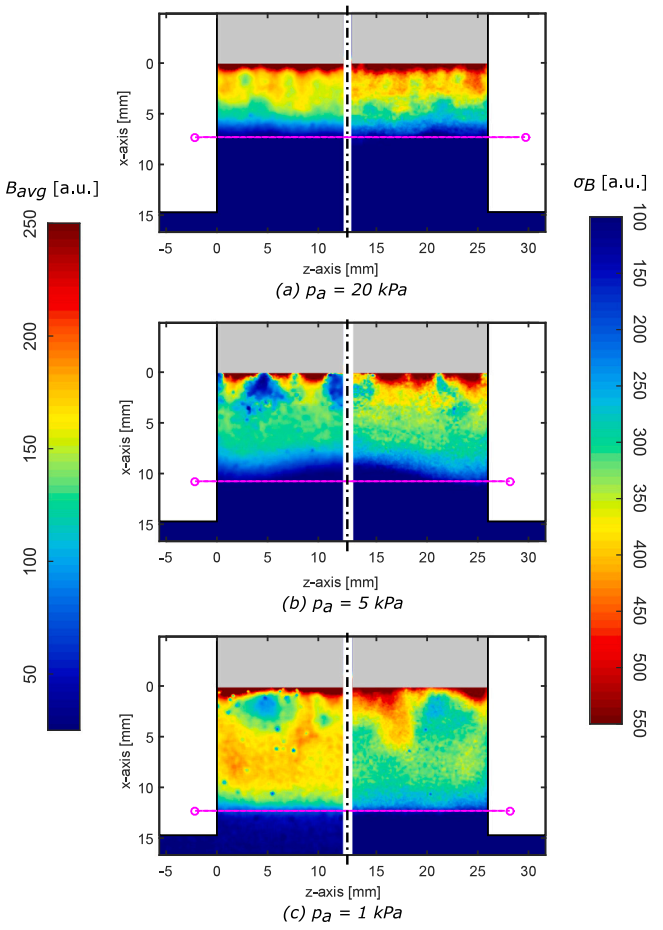

Fig. 4. Luminance of the plasma discharge: time-averaged image B_{avg} on the left, and temporal standard deviation image σ_B on the right as a function of the vacuum level p_a, i.e., p_a = 20 kPa (a), p_a = 5 kPa (b), and p_a = 1 kPa (c).

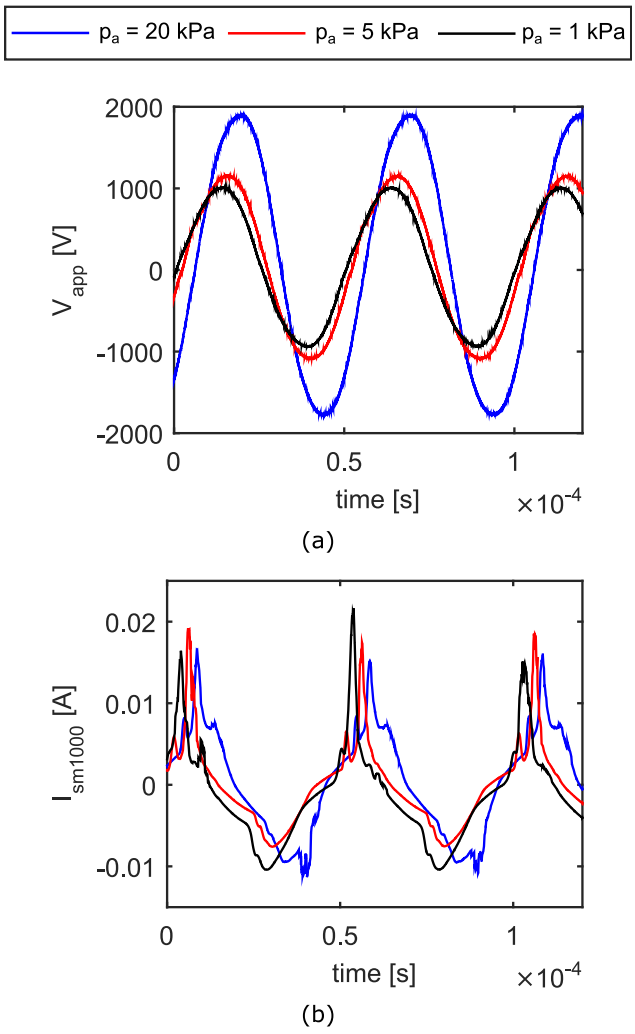

Fig. 5. Signals of the applied voltage (V_{app}) and the electrical current after smoothing using moving average window of size equal to 1000 samples (I_{sm1000}) as a function of the vacuum level p_a from 20 kPa to 1 kPa.

the same power supply setting. Thus, the peak-to-peak current also reduces with the vacuum level, mostly due to the gas rarefaction effect and, hence, the lower density of the ionized gas; the average electrical dissipated power $P_{el,avg}$ reduces too in accordance with the lowering of V_{pp} and I_{pp}. On the contrary, the average discharge power density $p_{pd,avg}$ increases by increasing the gas rarefaction, outlining that the energy per unit mass deposited into the discharge at 1 kPa is about 3.69 times the one deposited into the discharge at 20 kPa. This result couples with the extension of the discharge length L_{pd}, which is 7.3 mm at 20 kPa and it increases up to cover the entire region between the electrodes at 1 kPa, suggesting the advantageous use of larger ground electrodes to further extend the actuation region.

The modification of the plasma discharge morphology is evinced from Fig. 4. At 20 kPa, the plasma discharge is mainly governed by the formation of multiple micro discharges on the exposed electrode edge propagating downstream in larger structures equally distributed along the spanwise direction (the positive current regime in Fig. 5(a)). They finally collapse in a glow discharge (the negative current regime in Fig. 5(b)).

This results in a momentum addition into the neutral background gas which is mainly unidirectional along the x-axis. At 1 kPa, the plasma discharge formation is not driven anymore by the propagating electrical sparks, but the glow discharge forms immediately after the micro discharges close to the exposed electrode, and develops on the SDBD-PA surface from the centre and the sides. This is clearly shown by the green-cyan-blue coloured region of B_{avg} in Fig. 4(c) denoting a weaker plasma discharge.

This is also confirmed by the current signal (black curve in Fig. 5(b)), which is characterized by a negative current regime longer than the positive current regime, while the voltage signal in Fig. 5(a) preserves its symmetry. It is worth underlining that the structure of the glow

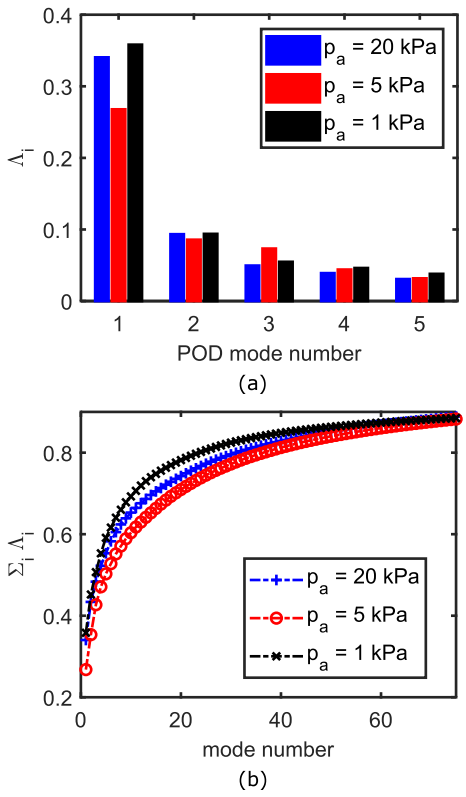

Fig. 6. Relative (a) and cumulative (b) energy of POD modes 1–3 as a function of the vacuum level p_a.

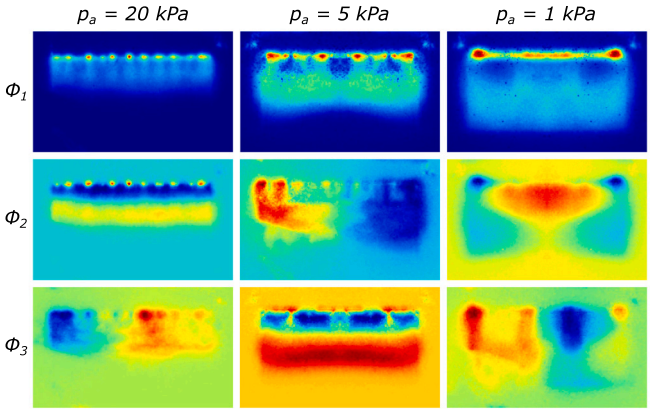

Fig. 7. POD eigen-structures of modes 1–3 as a function of the vacuum level p_a.

discharge established at 1 kPa is not anymore unidirectional, which suggests that the momentum addition into the neutral background gas occurs in the SDBD-PA plane (both x and y axes).

The plasma discharge at 5 kPa figures out the transition between the spark-driven plasma discharge at 20 kPa and the glow-driven plasma discharge at 1 kPa. This is clearly outlined in the POD analysis. The POD relative energy of modes 1 in Fig. 6(a) significantly drops down, as well as the cumulative energy (red curve in Fig. 6(b)) lowers down. The plasma discharge transition is also highlighted by the eigen-structures in Fig. 7. The first mode consists of a single oscillating coherent structure at all vacuum levels, in accordance with the standard deviation maps previously described. However, modes 2 and 3 consist of multiple coherent structures cyclically alternating based on the temporal eigenfunctions shown in Fig. 8.

At p_a = 20 kPa, mode 2 has two main structures developed along the span-wise direction (z-axis): the first one (blue structure in Fig. 7) is attached to the exposed electrode and the second one (yellow structure in Fig. 7) is placed immediately downstream. These structures spatially define the main plasma discharge cycle occurring into two main stages. It is worth observing the presence of 11 red spots on the exposed electrode edge: they identify the plasma discharge inception points, confirming that the plasma discharge originates in these points and then becomes a more uniform plasma sheet. Mode 3 owns two main big structures developed along the x-direction. They are located over the grounded covered electrode on the left and on the right of the longitudinal (from the exposed electrode to the grounded covered electrode) axis of symmetry, denoting lateral modal dynamics of the plasma discharge. Because of this, these structures are likely related to the spark-type discharge regime formed when the electrical current is positive. The doublet structures of modes 2 and 3 extend and invert at p_a = 5 kPa, remarking the plasma discharge transition observed in the modal energies: mode 2 owns the spark-type lateral dynamics, while mode 3 exhibits the glow-type longitudinal dynamics. At p_a = 1 kPa, mode 2 owns alternating longitudinal and lateral dynamics: the red structure forms on the centre of the exposed electrode edge and longitudinally propagates from the centre towards the sides; the blue one originates on the two lateral vertexes of the exposed electrode edge and propagates from the sides towards the centreline. It is also observed that the plasma discharge inception region in mode 1 is less discrete than retrieved in mode 2 at p_a = 20 kPa, with smaller inception points more evenly distributed along the exposed electrode edge.

The temporal evolution of the POD structures is described by the temporal eigenfunctions in Fig. 8, where the red lines denote the smoothing of the POD-retrieved signals (blue curves), using moving average windows of size equal to 15 samples.

The most characteristic temporal dynamics is outlined by mode 1, in accordance with the image luminance density signal $\rho_{B>50,sm15}$ shown in Fig. 9. They figure out the presence of a low-frequency content at p_a = 20 kPa of about 650 Hz, which increases to about 2500 Hz at p_a = 1 kPa. This low-frequency periodic behaviour is not retrieved at p_a = 5 kPa, remarking again the occurrence of a transitional regime characterized by a stronger spark-induced behaviour with high positive and negative peaks and smoothed signal weakly oscillating close to the zero without a characteristic periodicity (see mode 2 in Fig. 8).

4.2. High vacuum: 1100 Pa to 0.01 Pa

Below 1 kPa the plasma discharge exhibited a significant modification becoming volumetric, which made it impossible to use the iCCD because of the inadequate focus. Furthermore, the plasma discharge exhibited several plasma instabilities in a narrow vacuum range from a few pascals to tens of pascals, which made it difficult to control the plasma regime. Therefore, a transient analysis carried out by continuously reducing the pressure into the vacuum chamber was performed to get preliminary insight concerning the modification of the plasma discharge at high vacuum conditions in support of next future investigations. To this purpose, a red-green-blue digital camera was used (frame speed equal to 30 fps), together with the electrical acquisitions.

As shown in Figs. 10(a) and 11(a), the voltage signal loses its sinusoidal shape at vacuum level lower than 1 kPa. In particular, below 50 Pa the positive voltage regime has a truncated peak, making the positive regime longer than the negative regime. Concerning the current signals in Figs. 10(b) and 11(b), the positive peaks related to the electrical sparks weaken as the vacuum level decreases and they disappear below 50 Pa, highlighting that the plasma discharge becomes increasingly glow type. This is confirmed in Fig. 12 showing the different plasma extension regimes vs the chamber pressure level (1100 to 0.01 Pa).

At a higher pressure regime (1.1 kPa), the discharge consists of a thin and well-distributed plasma above the dielectric over the ground

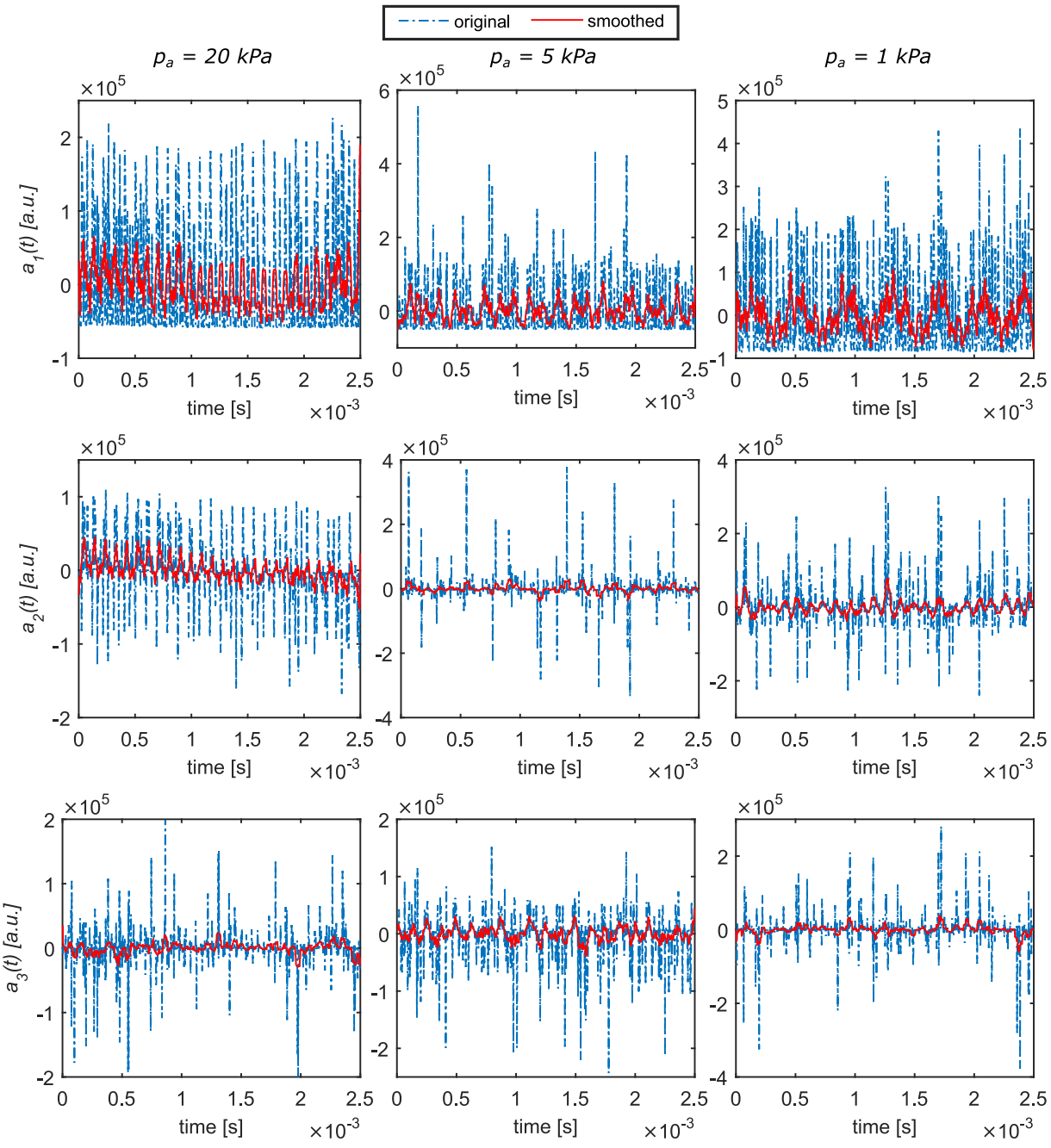

Fig. 8. POD temporal eigenfunctions of modes 1–3 as a function of the vacuum level p_a.

area. When the chamber pressure starts to decrease below 1 kPa, the discharge character is modified, and the discharge moves towards increasingly high vacuum operation [35]. With the decrease of the residual pressure, the thickness of the plasma layer remains unchanged up to approximately 500 Pa. Experimental observations showed that the SDBD plasma layer starts to expand to the volume above the glass over the ground electrode at a pressure below 2.5 Pa, losing its confined boundaries at about 1 Pa (glow light in the whole chamber). Some light spots on the electrode's edges are visible.

Table 3 reports the electrical performance acquired during the experiment (only one acquisition was performed per vacuum level due to the transient nature of the test and, for this reason, such quantities are not averaged values). The modification of the plasma discharge regime previously discussed is also retrieved by the electrical dissipated power P_{el}: between 1100 Pa and 50 Pa, P_{el} is positive and reduces with the vacuum level as expected. However, below 50 Pa, a fast modification of the plasma discharge occurs returning stable below 2.5 Pa (third picture from the left in Fig. 12). The new plasma discharge regime (pure glow type) is characterized by weakly negative electrical dissipated power, increasing V_{pp} and I_{pp}, while f_{elec} is almost constant and equal to about 20 kHz. It is worth observing that the relative uncertainty of P_{el} increases from 5% at 1100 Pa to a maximum of about 67% at 2.5 Pa as P_{el} approaches zero watts. At lower p_a, the relative uncertainty reduces again up to 34% at 0.01 Pa.

As already reported, below 2.5 Pa, plasma consists of a volumetric full glow type, with a stronger action on the exposed electrode where a higher plasma density has been evaluated. Fig. 13 shows the plasma effects on the exposed HV-electrode, through surface modifications evidenced by tungsten thin film with different colours vs the streamwise direction.

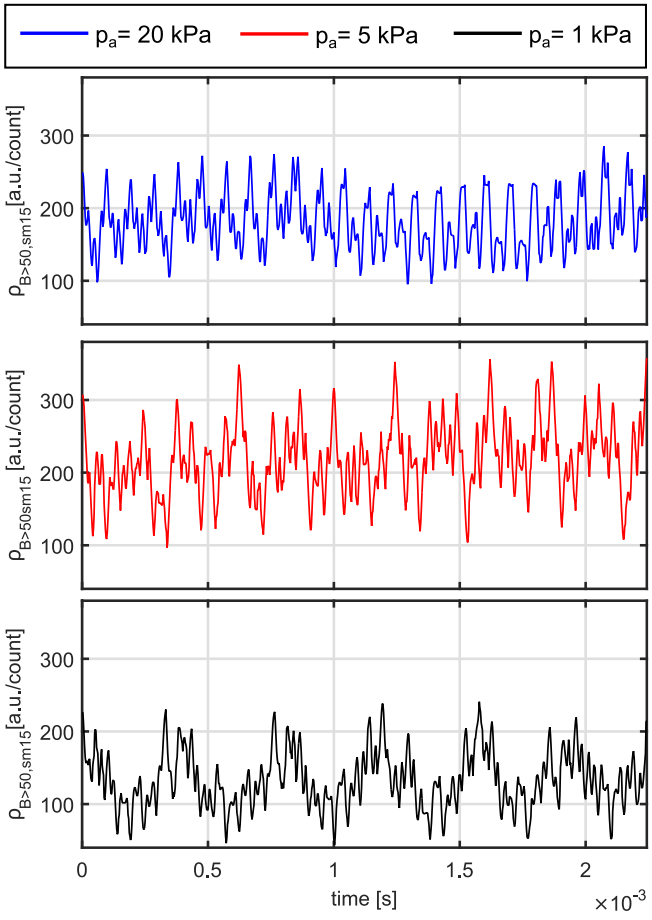

Fig. 9. Image luminance density signal $\rho_{B>50,sm15}$ as a function of the vacuum level p_a.

Table 3
Electrical performance of the SDBD-PA as a function of the vacuum level p_a from 1100 Pa to 0.01 Pa: dissipated power P_{el} and its absolute uncertainty δ_P, peak-to-peak voltage V_{pp} and its absolute uncertainty $\delta_{V_{pp}}$, and peak-to-peak current I_{pp} and its absolute uncertainty $\delta_{I_{pp}}$. Actuation frequency $f_{elec} = 20.1$ kHz.

p_a	V_{pp}	$\delta_{V_{pp}}$	I_{pp}	$\delta_{I_{pp}}$	P_{el}	δ_P
[Pa]	[kV]	[kV]	[mA]	[mA]	[W]	[W]
1100	2.53	±0.06	57	±2	1.40	±0.07
480	1.90	±0.04	20	±1	1.29	±0.05
50	1.44	±0.04	11	±1	0.59	±0.03
2.50	1.68	±0.04	5.1	±0.7	−0.03	±0.02
1.30	2.07	±0.04	5.8	±0.7	−0.05	±0.02
0.83	2.34	±0.04	6.2	±0.7	−0.06	±0.02
0.60	2.60	±0.04	7.8	±0.7	−0.08	±0.02
0.01	2.83	±0.04	10.4	±0.7	−0.06	±0.02

These zones have been investigated by Atomic Force Microscopy analysis with the aim to verify a possible correlation between coloured fringes and different surface morphology and roughness. The influence of plasma bombardment on HV electrode and glass substrate roughness is summarized in Fig. 14. The overall effect of the plasma on HV electrode is a more pronounced surface roughness in the HV edge located on the ground electrode side where the degradation effects are evident. In this area (blue and yellow fringes) the root mean square roughness reaches the highest values between 14.6 ± 1.4 nm and 14.9 ± 1.6 nm. Far from the ground electrode edge, the roughness is lower, and it decreases down to 11.4 ± 1.3 nm. This result evidences different intensity in the activity of the energetic particles along the HV electrode area during the bombardment of the surface, probably due to the plasma instabilities detected at low pressure (previously discussed).

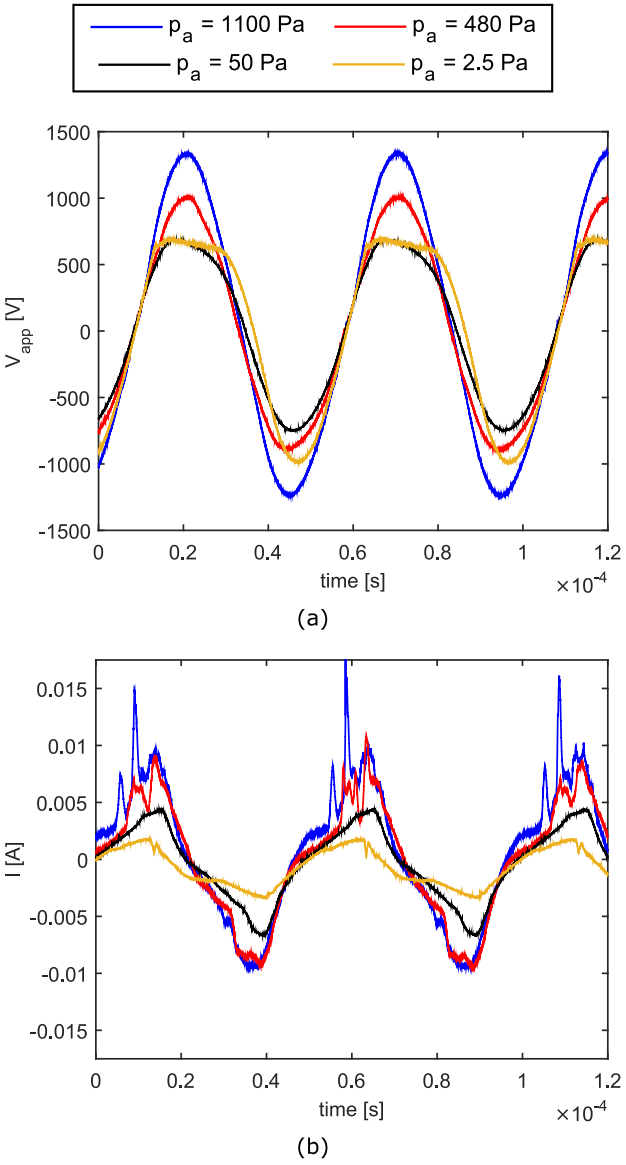

Fig. 10. Characteristic curves of the applied voltage V_{app} (a) and electrical current I (b) as a function of the vacuum level p_a from 1100 Pa to 2.5 Pa.

On the contrary, the glass roughness is almost constant over the entire ground area at about 4.7 ± 1.1 nm. No delamination or totally eroded areas have been observed on HV electrode after 6 h of operation, which makes the proposed technology applicable to active flow control at typical vacuum levels in space systems.

5. Conclusions

The behaviour of the plasma discharge produced by an SDBD-PA is still unexplored under typical gas rarefaction conditions of near-space applications with pressures below a few kilopascals. Furthermore, the gas-rarefied condition and the consequent collisional phenomena significantly increase the complexity of the physics and chemistry involved in such a plasma discharge. This couples with the need for reduced order models of SDBD-PAs to improve the predictability of the plasma discharge, which requires experimental data to be processed with techniques which can extrapolate the most relevant information into the domains of space–time–frequency. In such a context, the present work provides an experimental characterization of the plasma discharge of a

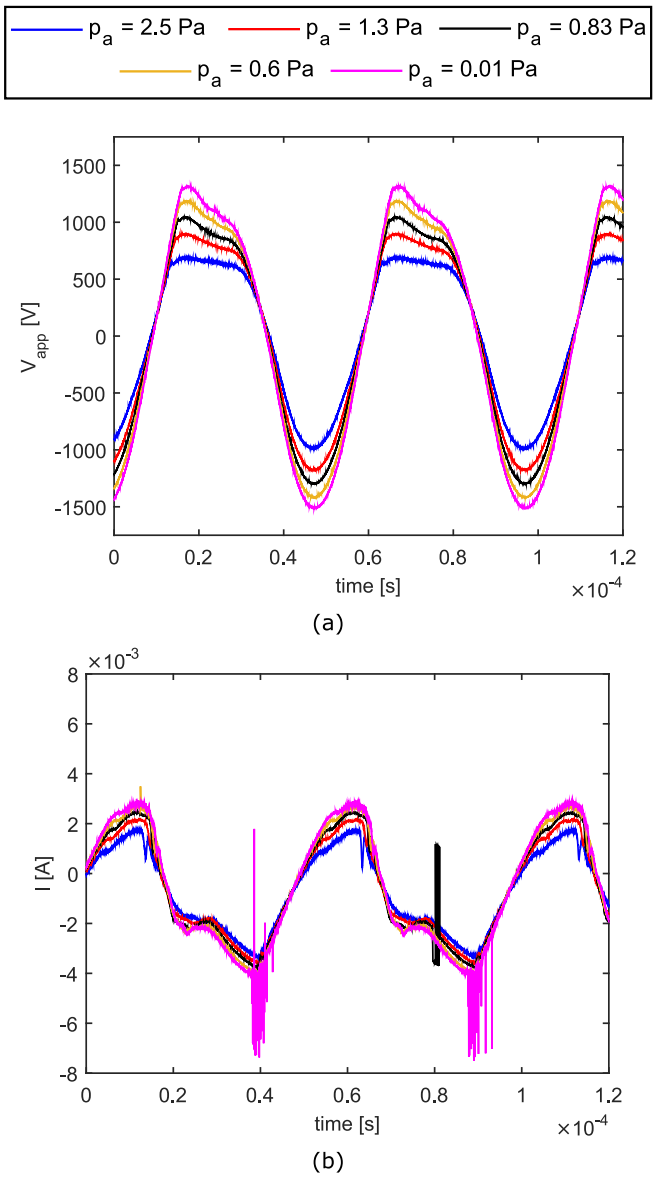

Fig. 11. Characteristic curves of the applied voltage V_{app} (a) and electrical current I (b) as a function of the vacuum level p_a from 25 Pa to 0.01 Pa.

novel SDBD-PA operating in typical vacuum conditions of air-breathing electric space vehicles. The device is manufactured via ultraviolet lithography CMOS processes, enabling advanced device engineering via the integration of a titanium nitride coating over the tungsten high-voltage electrodes to mitigate their degradation and extend the device's lifetime. Experiments have been performed in a vacuum chamber by considering two vacuum ranges: intermediate vacuum from 20 kPa to 1 kPa in steady-state conditions, and high vacuum from 1100 Pa to 0.01 Pa in transient conditions. Results highlight that at 20 kPa the plasma discharge is driven by the formation of micro sparks on the inner edge of the exposed electrode, which propagate downstream in larger current structures. At 1 kPa, the plasma discharge becomes more glow-type with negative current regimes longer than the positive ones, while the voltage signals preserve their sinusoidal shape. In such a plasma regime, the discharge extends over the entire region covered by the electrodes, suggesting the use of larger/wider grounded electrodes to further enlarge the actuation region. Furthermore, the momentum action of the plasma discharge on the neutral background gas is not anymore unidirectional as it acts on the whole SDBD-PA plane in both x and y axes. At pressure between 50 Pa and 2.5 Pa, the plasma discharge is unstable exhibiting a fast modification of the plasma discharge. Below 2.5 Pa, it becomes volumetric full glow type, extending its action mainly upstream with higher plasma density on the exposed electrode. The establishment of the new plasma regime at pressure below 2.5 Pa is also retrieved in negative electrical dissipated powers and asymmetric shapes of both voltage and current signals. Future steps will focus on the introduction of force measurements into the vacuum chamber to provide a quantitative assessment of the control authority of the SDBD-PA, together with a more extensive investigation of the plasma discharge physics/chemistry, the device durability and the degradation phenomena due to plasma discharge-electrode interaction.

CRediT authorship contribution statement

D. Fontanarosa: Conceptualization, Methodology, Validation, Investigation, Formal analysis, Data curation, Visualization, Writing – review & editing. **M.A. Signore:** Conceptualization, Investigation, Resources, Writing – review & editing. **A.M. Toscano:** Formal analysis, Validation, Writing – original draft. **M.G. De Giorgi:** Conceptualization, Methodology, Investigation, Resources, Writing – review & editing, Supervision, Project administration. **E. Pescini:** Conceptualization, Methodology, Validation, Investigation, Formal analysis, Writing – review & editing. **A. Ficarella:** Funding acquisition. **L. Francioso:** Conceptualization, Methodology, Investigation, Resources, Writing – review & editing, Supervision, Project administration, Funding acquisition.

Declaration of competing interest

The authors declare that they have no known competing financial interests or personal relationships that could have appeared to influence the work reported in this paper.

Data availability

The authors declare that all research data supporting this study are available from the corresponding author upon reasonable request.

Acknowledgements

Special acknowledgement to the technical staff of CNR-IMM Concetta Martucci, Adriana Campa, Pasquale Cretí and Enrico Melissano for microfabrication processes support; to Flavio Casino for wafer bonding setup discussion and realization. This research was funded by the Italian Ministry of University and Research, project PON "CLOSE to Earth", Avviso MIUR n. 1735 del 13/07/2017 AVVISO PER LA PRESENTAZIONE DI PROGETTI DI RICERCA INDUSTRIALE E SVILUPPO SPERIMENTALE NELLE 12 AREE DI SPECIALIZZAZIONE INDIVIDUATE DAL PNR 2015–2020. All authors approved the version of the manuscript to be published.

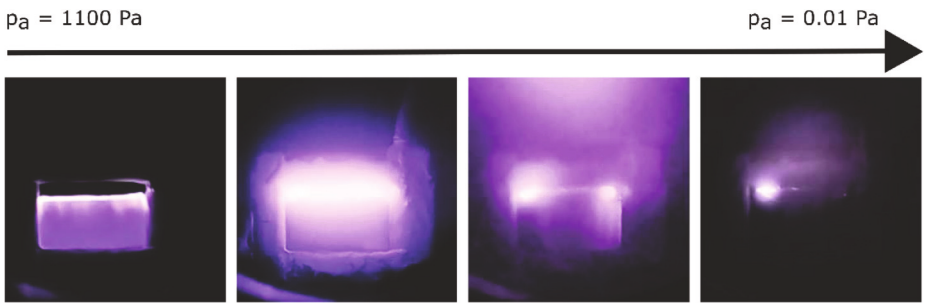

Fig. 12. Modification of the plasma discharge appearance as increasing the vacuum level p_a from 1100 Pa to 0.01 Pa.

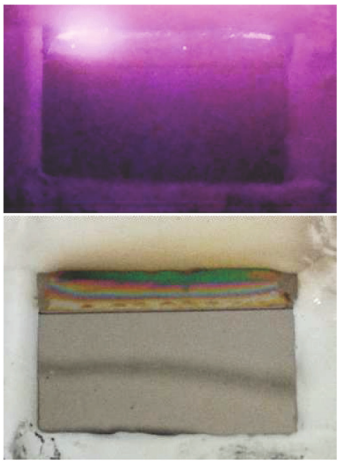

Fig. 13. Plasma discharge — SDBD-PA interaction at high vacuum conditions (p_a < 2.5 Pa): during testing (top) and after testing (bottom).

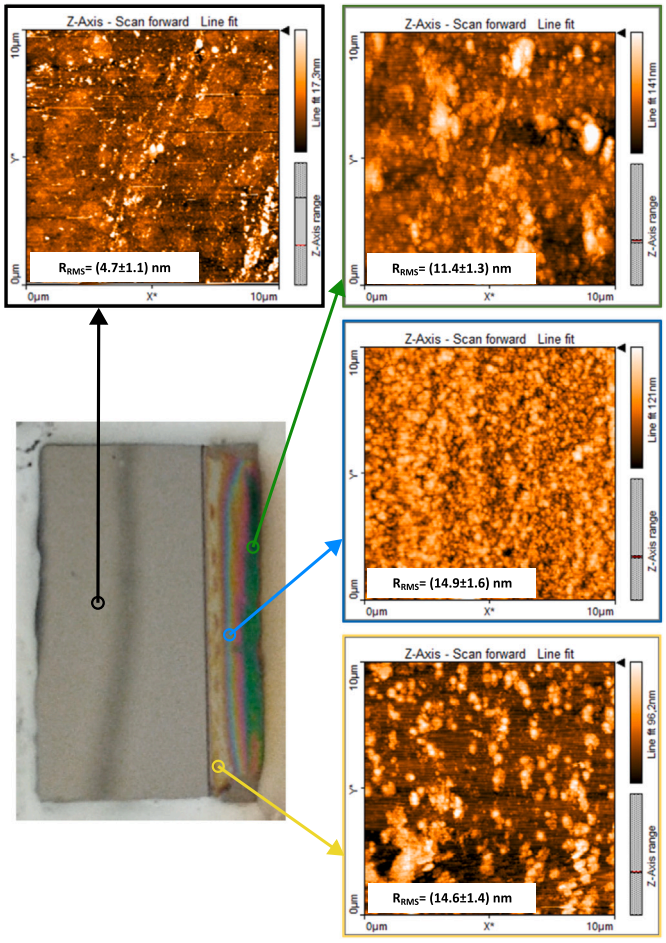

Fig. 14. AFM topography acquired in different areas of the HV-electrode and on the glass substrate.

References

[1] P. Chen, Z. Wu, X. Liu, K. Xie, N. Wang, An air-breathing electric thruster for near-space vehicle, J. Astronaut. 2 (2016) 203–208.

[2] D. Lev, R.M. Myers, K.M. Lemmer, J. Kolbeck, H. Koizumi, K. Polzin, The technological and commercial expansion of electric propulsion, Acta Astronaut. 159 (2019) 213–227, http://dx.doi.org/10.1016/j.actaastro.2019.03.058, URL https://www.sciencedirect.com/science/article/pii/S0094576518319672.

[3] A. Weiss, U.V. Kalabić, S. Di Cairano, Station keeping and momentum management of low-thrust satellites using MPC, Aerosp. Sci. Technol. 76 (2018) 229–241, http://dx.doi.org/10.1016/j.ast.2018.02.014, URL https://www.sciencedirect.com/science/article/pii/S1270963817311756.

[4] M. Manente, F. Trezzolani, M. Magarotto, E. Fantino, A. Selmo, N. Bellomo, E. Toson, D. Pavarin, REGULUS: A propulsion platform to boost small satellite missions, Acta Astronaut. 157 (2019) 241–249, http://dx.doi.org/10.1016/j.actaastro.2018.12.022, URL https://www.sciencedirect.com/science/article/pii/S0094576518310488.

[5] M. De Giorgi, D. Fontanarosa, A novel quasi-one-dimensional model for performance estimation of a Vaporizing Liquid Microthruster, Aerosp. Sci. Technol. 84 (2019) 1020–1034, http://dx.doi.org/10.1016/j.ast.2018.11.039, URL https://www.sciencedirect.com/science/article/pii/S1270963818320881.

[6] A. Cervone, A. Mancas, B. Zandbergen, Conceptual design of a low-pressure micro-resistojet based on a sublimating solid propellant, Acta Astronaut. 108 (2015) 30–39, http://dx.doi.org/10.1016/j.actaastro.2014.12.003, URL https://www.sciencedirect.com/science/article/pii/S0094576514005001.

[7] Z. Liwei, W. Liqiu, Y. Zhou, S. Changyou, L. Jingjing, Z. Desheng, D. Yongjie, L. Hong, T. Jingfeng, Time-domain signal analysis of dielectric response of nonlinear SDBD thruster in near space, Vacuum 207 (2023) 111666, http://dx.doi.org/10.1016/j.vacuum.2022.111666, URL https://www.sciencedirect.com/science/article/pii/S0042207X22007886.

[8] V. Khomich, V. Malanichev, I. Rebrov, Electrohydrodynamic thruster for near-space applications, Acta Astronaut. 180 (2021) 141–148, http://dx.doi.org/10.1016/j.actaastro.2020.12.002, URL https://www.sciencedirect.com/science/article/pii/S0094576520307360.

[9] M. Homaeinezhad, M. Nesaeian, Analytical model for corona discharge-based electrohydrodynamic plasma actuator incorporating environmental conditions, Acta Astronaut. 210 (2023) 224–236, http://dx.doi.org/10.1016/j.actaastro.2023.05.031, URL https://www.sciencedirect.com/science/article/pii/S0094576523002722.

[10] Y. Guan, R.S. Vaddi, A. Aliseda, I. Novosselov, Analytical model of electrohydrodynamic flow in corona discharge, Phys. Plasmas 25 (8) (2018) 083507.

[11] E. Pescini, D. Martínez, M. De Giorgi, A. Ficarella, Optimization of micro single dielectric barrier discharge plasma actuator models based on experimental velocity and body force fields, Acta Astronaut. 116 (2015) 318–332.

[12] D.F. Opaits, A.V. Likhanskii, G. Neretti, S. Zaidi, M.N. Shneider, R.B. Miles, S.O. Macheret, Experimental investigation of dielectric barrier discharge plasma actuators driven by repetitive high-voltage nanosecond pulses with dc or low frequency sinusoidal bias, J. Appl. Phys. 104 (4) (2008).

[13] L. Zhou, L. Wei, N. Song, D. Zhou, X. Yang, J. Tang, Y. Ding, H. Li, D. Yu, Effect of dynamic permittivity in low-pressure environment on performance of surface dielectric barrier discharge ion wind thruster, Vacuum 201 (2022)

111111, http://dx.doi.org/10.1016/j.vacuum.2022.111111, URL https://www.sciencedirect.com/science/article/pii/S0042207X22002391.
[14] T. Ukai, A. Russell, H. Zare-Behtash, K. Kontis, Temporal variation of the spatial density distribution above a nanosecond pulsed dielectric barrier discharge plasma actuator in quiescent air, Phys. Fluids 30 (11) (2018).
[15] R. Erfani, T. Erfani, S.V. Utyuzhnikov, K. Kontis, Optimisation of multiple encapsulated electrode plasma actuator, Aerosp. Sci. Technol. 26 (1) (2013) 120–127.
[16] J.W. Bradley, J.-S. Oh, O.T. Olabanji, C. Hale, R. Mariani, K. Kontis, Schlieren photography of the outflow from a plasma jet, IEEE Trans. Plasma Sci. 39 (11) (2011) 2312–2313.
[17] J. Xu, Z. Wu, P. Chen, Q. Xia, K. Xie, X. Liu, Parametric study of an air-breathing electric propulsion for near-space vehicles, J. Propuls. Power 34 (5) (2018) 1297–1304, http://dx.doi.org/10.2514/1.B36131.
[18] R. Erfani, H. Zare-Behtash, C. Hale, K. Kontis, Development of DBD plasma actuators: The double encapsulated electrode, Acta Astronaut. 109 (2015) 132–143.
[19] R. Erfani, H. Zare-Behtash, K. Kontis, Influence of shock wave propagation on dielectric barrier discharge plasma actuator performance, J. Phys. D: Appl. Phys. 45 (22) (2012) 225201.
[20] M.M. Wojewodka, C. White, T. Ukai, A. Russell, K. Kontis, Pressure dependency on a nanosecond pulsed dielectric barrier discharge plasma actuator, Phys. Plasmas 26 (6) (2019).
[21] M. Homaeinezhad, M. Nesaeian, Analytical model for corona discharge-based electrohydrodynamic plasma actuator incorporating environmental conditions, Acta Astronaut. 210 (2023) 224–236.
[22] J. Xu, Z. Wu, P. Chen, Q. Xia, K. Xie, X. Liu, Parametric study of an air-breathing electric propulsion for near-space vehicles, J. Propuls. Power 34 (5) (2018) 1297–1304.
[23] E. Moreau, N. Benard, J.-D. Lan-Sun-Luk, J.-P. Chabriat, Electrohydrodynamic force produced by a wire-to-cylinder dc corona discharge in air at atmospheric pressure, J. Phys. D: Appl. Phys. 46 (47) (2013) 475204, http://dx.doi.org/10.1088/0022-3727/46/47/475204.
[24] L. Zhou, L. Wei, N. Song, D. Zhou, X. Yang, J. Tang, Y. Ding, H. Li, D. Yu, Effect of dynamic permittivity in low-pressure environment on performance of surface dielectric barrier discharge ion wind thruster, Vacuum 201 (2022) 111111.
[25] N. Benard, N. Balcon, E. Moreau, Electric wind produced by a surface dielectric barrier discharge operating in air at different pressures: aeronautical control insights, J. Phys. D: Appl. Phys. 41 (4) (2008) 042002, http://dx.doi.org/10.1088/0022-3727/41/4/042002.
[26] J. Soni, S. Roy, Low pressure characterization of dielectric barrier discharge actuators, Appl. Phys. Lett. 102 (11) (2013) 112908.
[27] K. Bottelberghe, Z. Mahmud, Low-pressure effects on a single DBD plasma actuator, in: 48th AIAA Aerospace Sciences Meeting Including the New Horizons Forum and Aerospace Exposition, 2010, p. 550.
[28] Z. Wu, J. Xu, P. Chen, K. Xie, N. Wang, Maximum thrust of single dielectric barrier discharge thruster at low pressure, AIAA J. 56 (6) (2018) 2235–2241.
[29] Quartz AF32 eco - Technical data, 2022, https://www.pgo-online.com/intl/af32.html. (Accessed 23 December 2022).
[30] R.J. Moffat, Describing the uncertainties in experimental results, Exp. Therm Fluid Sci. 1 (1) (1988) 3–17, http://dx.doi.org/10.1016/0894-1777(88)90043-X.
[31] L. Sirovich, Turbulence and the dynamics of coherent structures, parts I, II and III, Quart. Appl. Math. (1987) 561–590.
[32] C. Tropea, A.L. Yarin, J.F. Foss, et al., Springer Handbook of Experimental Fluid Mechanics, Vol. 1, Springer, 2007.
[33] A.-M. Kypraiou, A. Dowling, E. Mastorakos, N. Karimi, Proper orthogonal decomposition analysis of a turbulent swirling self-excited premixed flame, in: 53rd AIAA Aerospace Sciences Meeting, http://dx.doi.org/10.2514/6.2015-0425.
[34] J.L. Lumley, The structure of inhomogeneous turbulent flows, Atmospheric Turbul. Radio Wave Propag. (1967) 166–178.
[35] J. Čech, Z. Bonaventura, P. Sťahel, M. Zemánek, H. Dvořáková, M. Černák, Wide-pressure-range coplanar dielectric barrier discharge: Operational characterisation of a versatile plasma source, Phys. Plasmas 24 (1) (2017) 013504, http://dx.doi.org/10.1063/1.4973442.